

# **Geriatric Rhinology**

a Computational Investigation

**Sean Read**



SAMME  
RMIT  
Australia  
Date

# **Abstract**

Abstract goes here

# **Dedication**

To Mum and Dad, Chris, Coka, Gary, Paper & Leigh

# **Declaration**

I declare that..

# Acknowledgements

I want to thank my supervisors, Dr Kiao Inthavong and Professor Jiyuan Tu and my cat

# Contents

<b>1</b>	<b>Introduction</b>	<b>7</b>
1.1	Background . . . . .	7
1.2	Research questions and objectives . . . . .	8
1.3	Research outline . . . . .	9
<b>2</b>	<b>Literature review</b>	<b>10</b>
2.1	Geriatric rhinology . . . . .	10
2.2	Experimental . . . . .	10
2.3	Computational Fluid Dynamics . . . . .	11
2.4	Airflow structures . . . . .	12
2.5	Demographic studies . . . . .	13
2.6	Heat and vapour transfer . . . . .	13
2.7	Literature gap . . . . .	14
<b>3</b>	<b>Model Reconstruction and Meshing</b>	<b>15</b>
3.1	geometry . . . . .	15
3.1.1	Introduction . . . . .	15
3.1.2	Non-invasive Medical Imaging . . . . .	15
3.1.3	Image Segmentation . . . . .	16
3.1.4	Preparation of Model for Meshing . . . . .	17
3.1.5	Summary . . . . .	18
3.2	Meshing . . . . .	18
3.2.1	Introduction . . . . .	18
3.2.2	Mesh Types . . . . .	18
3.2.3	Meshing algorithms . . . . .	19
3.2.4	Quality . . . . .	19
3.2.5	Mesh Independence . . . . .	20
3.2.6	Meshing of the Nasal Cavity . . . . .	20
<b>4</b>	<b>CFD fundamentals</b>	<b>21</b>
4.1	Fluid dynamics . . . . .	21
4.1.1	Mass Conservation . . . . .	21
4.1.2	Momentum Conservation . . . . .	22
4.2	Energy Conservation . . . . .	23

4.3	Governing Equations . . . . .	24
4.4	Heat Transfer . . . . .	24
4.5	Species Transport . . . . .	24
<b>5</b>	<b>Results</b>	<b>25</b>
5.1	Geometry Variations . . . . .	25
5.2	Pressure Drop . . . . .	26
5.3	Wall Shear Stress . . . . .	32
5.4	Velocity . . . . .	32
5.5	Heat and Vapour Transfer . . . . .	39
<b>6</b>	<b>Discussion</b>	<b>40</b>
<b>7</b>	<b>Conclusion</b>	<b>41</b>

# Chapter 1

## Introduction

### 1.1 Background

The ageing global population behooves a greater interest and investment in research and innovation in the area of geriatrics. One area of particular significance within the field of geriatrics is that of geriatric rhinology. A range of dysfunctions and aberrations from the normal functioning of healthy adults have been observed in the nasal cavities of elderly populations[4, 20]. These aberrations are liable to impact significantly on the quality of life of the sufferers. The nasal cavities of elderly citizens have been shown by previous researchers to show increased volume[14]. Alterations in histiological function have also been shown[11]. The extent to which functional aberrations are caused by geometric variations remains unclear[34]. The occurrence of respiratory diseases in the elderly is markedly higher than that found in younger populations[11, 4]. It has been suggested that these higher recorded rates could be due in part to the impaired air conditioning functionality[20].

particle toxicology is an area which has been receiving increasing interest in recent decades. The potential health issues related to the inhalation of environmental hazards are multifarious and often life threatening. In order to minimise the physical cost to society of both man made and natural environmental toxins an understanding of the mechanisms by which the contaminants are being introduced in to the human body is imperative.

The use of computational fluid dynamics (CFD) to analyse nasal cavity flow dynamics is an area which has been receiving significant research attention in recent years. CFD simulations allow the achievement of highly detailed results with information covering a range of areas for a given fluid system at a minimal cost. Some of the more significant areas The use of 3d medical imaging techniques such as computed tomography (CT) scans in collaboration with CFD has facilitated the use CFD modeling techniques to approximate numerically fluid mechanism parameters of anatomically accurate models taken from models produced *in vivo*. This allows for more detailed comparisons of the effects

of topological variations on the relevant fluid mechanisms.

The analysis of highly accurate models facilitated by the use of ct scans presents an opportunity for the analysis of inter-demographic variations in nasal cavity functionality. To date numerous inter-demographic studies have been carried out using CFD analysis of 3d models reconstructed from ct scan data. These demographic studies have included several focusing on age, however these age related studies have all focused on the variations between children and adults.

## 1.2 Research questions and objectives

In light of the information posed above, the following questions seem pertinent:

- How do changes in nasal cavity geometry - caused by age - influence its airflow mechanisms?
- How do the same changes impact on heat and vapour transfer within the cavity?

To answer the aforementioned questions, the following objectives have been outlined:

- reconstruct a series of nasal cavity geometries from medical scans that represent a spread of geometric characteristics [such as volume and surface area] across the norm. The existing literature shows a clearly defined relationship between age and volume: these models will serve as a representation of the aging population to be analysed computationally.
- Model airflow across the series of reconstructed nasal cavities using computational fluid dynamic using a steady state assumption; defining inlet conditions to approximate a resting rate of respiration.
- Compare the simulation results between geometries. A variety of post processing methods have been employed to compare various aspects of fluid mechanic functionality of the nasal cavity models. The literature has shown clear discrepancies in the functionality of nasal cavities as a function of age; it is our intention through these measurements to examine in more detail the extent of these variations.
- Compare results with existing results from various experimental methods from the previously extant literature. The results of the post processing Will be used to explain discrepancies in nasal functionality observed by previous researchers.

### **1.3 Research outline**

Developments medical image reconstruction technologies now allow researchers to reconstruct highly detailed, digital 3d representations of various anatomical structures from ct scans. When coupled with CFD simulations, this presents an unprecedented capacity for in depth analysis of physiological fluid flow mechanisms.

This study aims to use CFD analysis of CT scan data from the nasal cavities of a range of Asian males to investigate the impact of the age induced expansion of the nasal cavity on the air-conditioning functionality of the nasal cavity. Air flow mechanisms, heat transfer rates and humidification efficacy is analysed. The Data is then discussed - in the context of the rhinological symptoms attributed by previous researches to elderly patients - in order to arrive at a more precise understanding of the role of nasal geometry in the presentation of said symptoms.

This study represents, to the best of our knowledge, the first in depth, mechanistic, computational study undertaken into the role of nasal geometry in common rhinological symptoms associated with the aging process.

# **Chapter 2**

## **Literature review**

### **2.1 Geriatric rhinology**

The common rhinological complaints of the elderly include dryness, runny noses, crusting and epistaxis[34]. Epidemiological studies have been carried out to examine the consistency of the manifestation of various symptoms throughout elderly patients with mixed results. The literature at present seems to be unanimous on the tendency of the nasal cavity's cross sectional area to increase with age. Several researchers have investigated this phenomena using acoustic rhinometry and shown good concordance in study outcomes[14, 4, 38, 20]. Nasal air heating and humidification have been examined vivo and shown to be impacted by age[20]. Increases in postnasal drip, nasal drainage, sneezing, coughing, olfactory dysfunction and gustatory rhinitis with age were observed in a clinical study of 131 patients[4]. The results on the impact of aging on the quality of life have not been unanimous, a 2009 study found that in a sample of 80 people no significant relationship could be observed between age and nasal discomfort[21]. The same study, however, concurred with previous results on the increase of volume and cross sectional area as a function of age. Changes with in the nose appear to not be limited to the increased volume. Both functional and structural variations in the respiratory epithelium have been observed with age, contributing to slower clearing of the mucous[11]. Functional variations in air conditioning capabilities have been shown in vivo[20], with statistically significant reductions in relative humidity and heat transfer observed in elder nasal cavities. The level to which this is attributable to change in histological function as opposed to variations in the fluid mechanisms as a result of the expansion of the cavity remains to be investigated.

### **2.2 Experimental**

The anatomy of the nasal cavity was first classified in detail by Emil Zuckerkandl in the 19th century[30]. Anatomically, his records were more or less up

to the standard of what can be assessed from modern scanning techniques[30], however the investigation of airflow characteristics was still severely limited by technological capacity[3]. It was not until the turn of the 19th century that experimentation in to nasal airflow began in proper[3]. The experimental methods used to examine airflow in the human nasal cavities in the last century have been numerous. Some of the more common *in vivo* techniques used include rhinomanometry, which allows measurement of the pressure drop across the nasal cavity[10] and acoustic rhinometry, which allows measurement of the cross sectional area of the nasal cavity as a function of depth[10]. Ultimately, however, direct detailed measurements of flow mechanics within the human nasal cavity taken *in vivo* are not viable with current technology as a result of the complexity and small scale of the nasal geometry[2]. Thus the preferred media for the testing in modern times has tended to be either physical or computational models reconstructed from ct scan data[2]. The physical models that have been constructed from ct scan data are able to provide high detail on fluid flow properties when compared with older techniques such as rhinomanometry[23], however such experimental set ups are costly to run in terms of time and resources, in particular when compared with the high level of detail that can be achieved from a well done CFD simulation[23].

### 2.3 Computational Fluid Dynamics

Computational fluid dynamics(CFDs) is a discipline which is principally concerned with the computational approximation of solutions to the navier stokes equations for closed fluid systems[33]. In many fields - inclunding rhinology - CFD has facilitated economical and detailed investigations in to cases in which experimental investigation would otherwise be costly or, in cases such as rhinology, impossible[17].

CFDs were the primary driving force behind the development of larger and faster computers until the 80's[37]. In more, recent times, the continuing advancement of computational technologies has facilitated considerable growth in the scope and accuracy of CFDs for predicting the behaviour of increasingly complicated systems[33].

One of the areas of investigation that has been facilitated by these advances is that of nasal airflow. Initially, simplified nasal cavity geometry models used to create computational meshes and solve numerically for the fluid flow properties under steady state conditions[17, 9]. Later 3D models extracted from CT scans were used to achieve more accurate results[25]. In addition to this, various inlet and outlet conditions have been compared, chiefly the difference between and unsteady which model the variations in flow as a function of time throughout the nasal cycle[29] or an assumed constant velocity, time independent, steady state assumption based model[36]. This discrepancy has been a point of much contention, and it seems that the current position is that this decision depends on the application at hand[2]. Certainly to date it seems that the vast bulk of the case studies comparing different geometries have used the steady state

assumption[39, 43, 7]

Another issue which has been of some debate in the literature is the relevance of the inclusion of sinuses in the modelled flow domain. It has been reasonably commonplace to include the sinuses in studies that are examining the effects of sinus surgery[41, 19]. Also it has been shown that, while the impact on airflow is relatively minimal, the sinuses can be subject to not insignificant levels of particle deposition for particles in the range of 1 nanometre in diameter, and particularly for low flow rates[8]. The added requirements in time and computational complexity necessitated by the inclusion of the sinuses, however, seems to warrant their exclusion from models in situations where they are not specifically relevant[2]

## 2.4 Airflow structures

Airflow structures have been investigated and portrayed through a variety of both qualitative and quantitative methods. The earliest papers prior to the widespread use of cfd's focused primarily on the pressure drop over the nostrils as measured with rhinomanometry[24]. Modern technological innovation has facilitated the development of a range of techniques for both visualisation of airflows and the quantification of their various characteristics. In particular the range of data that can be obtained from numerical simulations is vast and detailed, and so the question of how to interpret it becomes particularly important.

One more commonly used visualisation method is the use of streamlines cite fig streamlines, often coloured by velocity[36, 43, 7]. These are useful for showing flow distribution as well as significant recirculation zones[22, 40]. Another commonly used method, shown in figure ref fig velocity contours is coronal cross sectional contours portraying velocity These contours may or not include streamlines to help highlight the presence of vortices in the flow[36]. Another method, presented in [22] uses a  $\Delta$  criterion to trace the vortices present in the flow structure. In [22], these are then coloured by variables related to turbulence and vorticity in order to provide a deeper insight in to the vortex structure behaviour.

Quantitative methods for analysing and comparing air flow structures seem to be less standardised. Prior to the invention of modern imaging and investigative techniques, rhinologists relied on readings of cross sectional area and pressure from techniques such as rhinomanometry and acoustic rhinometry[2]. The detailed flow information that can be extracted from ct scan models either experimentally or computationally opens up a much wider range of options in terms of quantitative analysis. Pressure is still often included as it is said to provide an insight in to the inspirational efficiency of the cavities[22]. Pressure is often plotted as a function of flow rate in order to provide a point for validation by comparison with experimental set ups[36, 13]. In addition, it is can be analysed as a function of longitudinal position in order to gain an insight in to the relationship between the geometric variations and pressure drop[22].

Another common technique is velocity distribution measurement[17, 43, 22]. This can include a cross sectional zone by zone analysis[17, 43], which has been suggested to be useful for the measurement of the efficacy of olfaction[43], or by longitudinal sections[22, 32]. Another commonly used quantitative measure is wall shear stress. Wall shear stress is also analysed in a variety of different ways. Distributions are analysed longitudinally[36] and around the cross sectional parameter of the relevant chapter of the nasal cavity[1]. These measurements have been shown to be significant for predicting heat and mass transfer within the regions[32], and thus their longitudinal and parametric distributions are significant understanding the distribution of such mechanisms.

## 2.5 Demographic studies

To date the variation of nasal cavity functionality has been compared between several demographics have been investigated in the literature. The previously investigated demographics include age[39], which can then be subclassified into children[39] and the elderly[20]. Both of these have been investigated through both in vitro[35] and in vivo[14, 4, 38, 20] techniques. Child models have also been investigated computationally[39]. The variations that have been observed in children's nasal airway functionality has been suggested to be linked to particle filtration ability [39]. It seems plausible that this effect could be significant also in the case of elderly models. Cross sectional areas have been graphed as a function of radial position to compare the geometries of different models in many studies[39, 43, 20, 7]. Surface area has also been suggested to be significant metric in predicting flow behaviour, as surface area to volume ratios are expected to impact on the flow behaviour[39, 7] resistance across the nasal cavity, measured as pressure drop, is also often used as a predictor of flow behaviour within the nasal cavity[4, 20, 38]. Streamlines are a commonly used method for visualising flow structures in nasal cavity models[39, 7, 43]. Flow flux by section has also been used to identify variations in nasal functionality[43].

## 2.6 Heat and vapour transfer

Earlier investigations into the heat and vapour transport characteristics of the nasal cavity used a straight pipe model as a simplification of the nasal cavity geometry[12]. The first experiments involving real nasal cavity geometries were carried out in the 80s, using cast models taken from cadavers[28].

In vivo experiments into temperature variation across the nasal cavity have been done using various temperature measuring devices; modern experiments have tended towards using thermocouples because they are small and respond quickly[6]. For measuring humidity in vitro, modern researchers have tended towards the use of capacitative temperature sensors[15]. Detailed profiles of temperature and humidity throughout the nasal cavity have been presented by several past researchers[15].

CFD's have been used to simulate heat and vapour transfer in the nasal cavities with good accordance with experimental results[18]. Early simulations investigating heat and vapour transfer used a steady state assumption for inflow conditions[27]. Later, the effect of the nasal cycle on temperature distributions were investigated, showing significant variations in the nasal temperature distributions throughout the nasal cycle[5].

Cross sectional temperature contours have been used to visualise the distribution of temperature throughout the nasal cavity; this provides a clear way of visualising the distribution[26]. Sagittal heat flux contours have also been used to similar effect[31]. Heat flux, temperature, water flux and humidity have all been mapped as a function of sagittal position in the nasal cavity[7, 31, 42]. The nasal valve has been noted from these observations to be a region of particular significance to heat and vapour transfer mechanisms[31].

## 2.7 Literature gap

To date, to the best of our knowledge, although some research has been carried out on the effects of aging on nasal airflow, CFDs have not been used to examine in depth the influence of age related variations in nasal cavity geometry on flow structure or heat and vapour transfer characteristics.

## Chapter 3

# Model Reconstruction and Meshing

### 3.1 geometry

#### 3.1.1 Introduction

The reconstruction of nasal cavity model computer images - including discretisation for modeling with CFD - can be divided into 5 stages: image acquisition, data conversion, segmentation, refinement and meshing. Firstly medical imaging technologies are used to extract a series of pixelated slices, in which the various materials which make up the human body can be identified by variation in greyscale measurements. These slices are then interpolated to create a 3D structure of voxels (the 3D equivalent of a pixel).

The reconstruction of the nasal cavity geometries can be very time consuming and prone to human error. The improvement on and automation of the reconstruction process are areas of active research. This chapter presents an overview of the methods in current use for the various phases (mentioned above) by which a nasal cavity geometry is prepared for CFD analysis.

#### 3.1.2 Non-invasive Medical Imaging

There are various forms of medical imaging that can be used for the identification of the nasal cavity geometry. Here a brief overview of Computed Tomography (CT), the form of medical imaging used for the nasal cavity geometries presented in this thesis.

CT scans use a series of x-rays taken at regular intervals within the required region. x-ray scans use photons sent in beams through the region of interest. These photons interact differently with the material that they encounter depending on its density. Electronic detectors feed the photon pattern emitted from the body in question to a computer, which uses this information to create

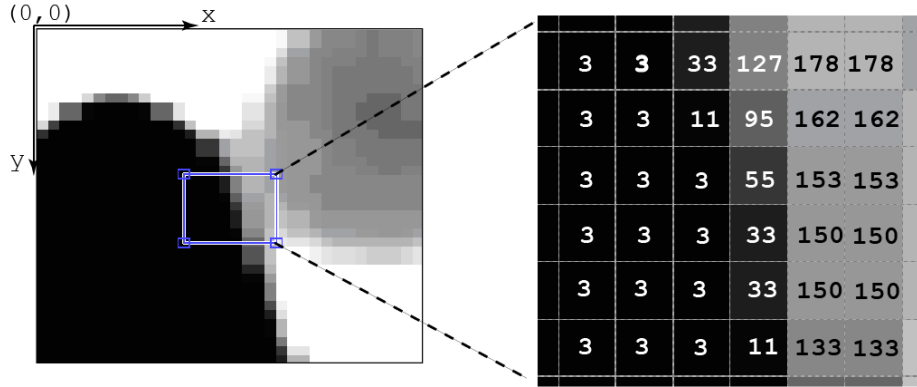


Figure 3.1: example of how greyscale values are assigned to pixels in a ct image

images. These images are made up of pixels which are each assigned a grey scale value based on their x-ray attenuation coefficient. In medical imaging the Hounsfield scale is used, whereas in image processing the greyscale is numbered from black to white between 0 to 255. Figure 3.1 shows an

### 3.1.3 Image Segmentation

Once the CT scan has been outputted as a series of voxels, the anatomical geometries relevant to the project at hand can be extracted. To achieve this goal, the voxels that make up the relevant chapter of the data need to be identified somehow. This can be done manually - by going through the many slices that make up the ct scan and identifying the relevant areas - however this process is extremely time consuming.

Numerous algorithms have been developed for the purpose of automating the process; all of which have certain advantages and disadvantages. For the most part these algorithms can be subsumed in to three categories, presented below (in order of increasing complexity):

- **Thresholding:** regions are identified and separated according their greyscale value. This is the simplest algorithm for defining regions.
- **Edge detection:** either local maxima of the first derivative of intensity or zero values of the second derivative are used to identify region edges. Edge detection tends to reduce the noise when compared with thresholding
- **Region based:** regions are grown from the inside out. This produces more coherent regions, but is unable to detect regions that are segregated.

These methods and many more exist and are in active development. In addition, many of them are available for free online. The implementation of such algorithms and applying from first principles, however is quite a complex procedure. Fortunately many of these algorithms have already been implemented in

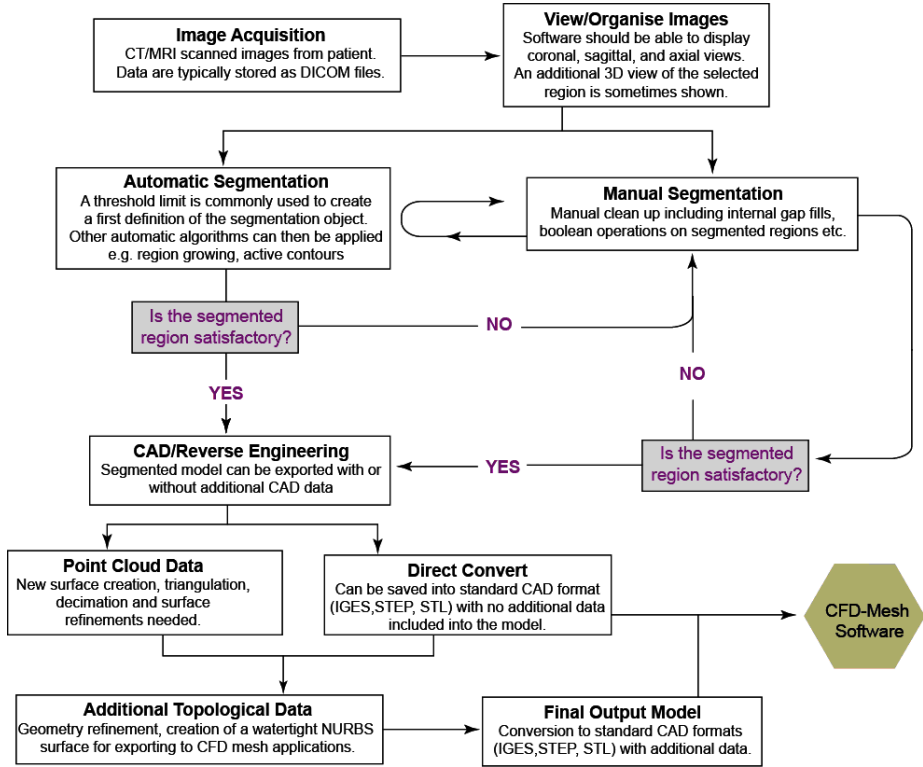


Figure 3.2: Flow chart showing the process by which an anatomical geometry is prepared - with the help of medical imaging - for modeling with CFDs

software packages - of which commercial and open source variations are available - which are specifically compiled for working with medical imaging outputs.

### 3.1.4 Preparation of Model for Meshing

Once the region in question has been extracted from the medical imaging output, it can be saved as some CAD format. There are certain criteria that need to be fulfilled by a CAD model before it can be read by 3d meshing software and used to create a mesh. It is often the case that when the data is exported from the medical imaging software is 'dirty'; that there are contradictory or arbitrary elements in the geometry. These elements need to be removed through the use of CAD software before the geometry is suitable for the creation of a useable 'clean' 3d mesh. Note that the geometry needs to contain also topological information in order to create a watertight mesh. The details of the process by which the geometry is prepared for meshing are described in Figure 3.2.

Figure 3.3: Example of nasal cavity geometry generation

### 3.1.5 Summary

Anatomical geometry reconstruction - including that of respiratory systems - begins with medical imaging of the area in question. The geometry is then extracted from the medical imaging data using one (or several) of the available extraction algorithms outlined above. After extraction, cleaning of the geometry with CAD software is generally necessary. It is necessary to ensure that the geometry is water-tight before it can be meshed. This chapter has given an overview of some of the more pertinent methods in current use for the reconstruction of anatomical geometries from medical imaging data. Figure 3.3 shows an example of the construction process.

## 3.2 Meshing

### 3.2.1 Introduction

The navier stokes equations, upon which Computational Fluid Dynamics is based (see chapter 4), is unsolvable (in most instances), except by approximation. A given geometry is approximated, or discretised, as a series of points. The process by which these points are defined and related to one another is known as meshing; this in itself is a complex discipline under active research. In this chapter current methods are reviewed, and guidelines are given for developing quality meshes.

### 3.2.2 Mesh Types

There are many types of mesh structure that can be employed; all of them have their own advantages and disadvantages.

- Structured meshes by definition, are divided into segments of uniform size and shape. It is characterised by cells posessing either four nodal corner points in two dimensions, or eight three. The points are mutually orthogonal and cartesionally defined. Being defined in this relatively simple way facilitates a higher level of computational efficiency. It is, however, limited in the level of structural complexity that it can accomodate.
- Unstructured Meshes The geometries encountered in the respiratory system are generally too complex to be effectively discretised in a structured manner; in cases such as these unstructured meshes can be used to accomodate the complexities of the given geometry. Unstructured meshes - usually constructed from triangles or tetrahedra - do not fit a regular pattern, and they do not have coordinate lines corresponding to curvilinear directions. Because of this, the solving of computations over unstructured

Figure 3.4: Examples of the mesh types described in section 3.2.2

domains is generally more computationally intensive, however with modern advances in computers this has become less significant an issue in many cases.

- Hybrid meshes One disadvantage to the use of unstructured meshes is that they tend to show less accuracy near the wall. One commonly applied solution is the use of hexahedral elements near the wall, with the rest of the volume filled with unstructured - usually tetrahedral - elements. This method tends to improve the accuracy of near wall computations. One draw back of this method is that the prism layers can break down in the vicinity of excessively contoured walls. In this study this is the mesh type that is employed.

### 3.2.3 Meshing algorithms

There are various meshing algorithms available, each with their own strengths and weaknesses. For the purpose of this study, an octree algorithm was selected. Octree algorithms work by repeatedly dividing The volume in to smaller sections, until the given criteria, for example mesh size, is fulfilled. This method is generally considered to be a relatively simple but robust approach to mesh generation. One drawback, however is that it can cause irregular element distributions near the boundary.

### 3.2.4 Quality

The quality of a generated mesh is dependant on its warp angle, skewness and aspect ratio. For a quadrilateral cell, as shown in figure 3.5, the aspect ratio of the cell is defined as  $AR = \frac{\Delta y}{\Delta x}$ . Within the interior region, the  $AR$  should be maintained within the range  $0.2 < AR < 5$ . This can be somewhat relaxed, however, in the vicinity of the wall.

Mesh skewness is defined as the extent to which it deviates in shape from the ideal. This is a square for quadrilateral cells, or an equilateral triangle for triangle or tetrahedral cells. It is simple quantified for triangles and tetrahedrals as  $\frac{\theta_{ideal} - \theta_{actual}}{\theta_{ideal}}$  (see figure 3.5 for theta).

For unstructured mesh, the warp angle (shown in figure ??) should be kept below  $75^\circ$ .

Many grid generation packages contain specific algorithms and/or functions for improving mesh quality. The gradient of mesh size variation should not exceed 1.2, as higher variations can cause problems in convergence.

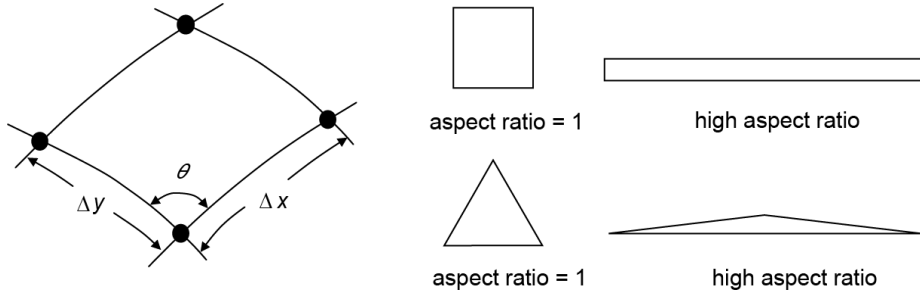


Figure 3.5: Example of mesh cell with spacing  $\Delta x$ ,  $\Delta y$  and angle  $\theta$  between the grid lines along with high  $AR$  triangular and quadrilateral elements

Figure 3.6: mesh independence

### 3.2.5 Mesh Independence

A significant source of error in the solution of CFD problems is derived from the discretisation process; when a system is separated into a number of finite elements, for the purpose of Numerical solution, the solution that is obtained from its solution is an approximation. It is necessary, then, to ascertain the required resolution, or mesh size, required to calculate a result that approximates the exact solution to a satisfactory degree of accuracy. This is done by means of a mesh independence test. This entails the monitoring of one - or several - fluid flow parameters of interest to the study over a series of mesh sizes. Independence is said to have been achieved when the effect of mesh size on the selected flow variable(s) has become insignificant. Figure 3.6 shows the results from the mesh independence test conducted for two of the five models presented in this thesis.

### 3.2.6 Meshing of the Nasal Cavity

In this section the relevant aspects of the theory behind mesh generation have been introduced. Figure 3.7 shows the meshing process applied to one of the nasal cavities geometries presented in this thesis. Note the use of hybrid mesh, with internal tetrahedral elements and close to wall prism layers, shown clearly in the cross sections. Also, note that the geometry has been previously cut into sections relevant to the planned analysis in the CAD refinement stage.

Figure 3.7: mesh generation process

# Chapter 4

## CFD fundamentals

### 4.1 Fluid dynamics

The aim of Computational fluid dynamics is to approximate numerically the physical conservation laws of newtonian physics:

- conservation of mass
- The conservation of momentum (Newtons second law, the rate of change of momentum equals the sum of forces acting on the fluid);
- The conservation of energy (first law of thermodynamics, the rate of change of energy equals the sum of rate of heat addition to and the rate of work done on the fluid).

#### 4.1.1 Mass Conservation

The principle of conservation of mass is that, in a closed system, the mass remains constant. This means that fluid will move through a set region in such a way the mass is conserved. For an incompressible flow, this means that the outflows and the inflows will be equal. This can be written as

$$0 = \sum_{in} \dot{m} - \sum_{out} \dot{m} \quad (4.1)$$

Where  $\dot{m}$  = mass flow rate.

The mass flow rate can be written as  $\rho u A$ , for  $\rho$  = density,  $u$  = velocity and  $A$  is the scross sectional area of the flow. For flow in the x direction,  $A = \Delta z \Delta x$ . For a two dimensional flow,  $\Delta z = 1$ , giving:

$$\dot{m}_{in} = \rho u \Delta y \quad (4.2)$$

Extending this to equation 4.1, in the x direction, for an incompressible flow we get

$$0 = \rho u_{in} \Delta y_{in} - \rho u_{out} \Delta y_{out} \quad (4.3)$$

This can easily be extrapolated to three dimensions.

In the case of the nasal cavity, this can be conceptualised in relation to the nasal cavity geometry

#### 4.1.2 Momentum Conservation

Momentum conservation is based on the Newton's second law,

$$\sum F = ma$$

Here  $m$  is the mass of the system,  $a$  is its rate of acceleration, and  $\sum F$  is the sum of forces acting on the system.  $F$  can generally be divided into body and surface forces. Rewriting the mass as the product of volume and the density, and acceleration as the first derivative of velocity:

$$\sum F_{body} + \sum F_{surface} = (\rho \Delta x \Delta y \Delta Z) \frac{DU}{Dt} \quad (4.4)$$

Body forces generally include gravity, centrifugal, Coriolis and electromagnetic forces; these all act on the volume from a distance.

Surface forces are those that act directly on the surface of a fluid element. These fluid forces include normal stress, in the  $x$  direction  $\sigma_{xx}$ , which is made up of pressure forces  $p$  exerted on the body and normal viscous stress components  $\tau_{xx}$ ; and tangential stresses,  $\tau_{xy}$  and  $\tau_{xz}$ .

Summing these forces in the  $x$  direction, for a 2D fluid element we get:

$$\begin{aligned} \sum F_{surface,x} &= [\sigma_{xx} \Delta y \Delta z - (\frac{\delta \sigma_{xx}}{\delta x} \Delta x) \Delta y \Delta z] \\ &\quad + [(\tau_{xy} + \frac{\delta \tau_{yx}}{\delta y} \Delta y) \Delta x \Delta z - \tau_{yx} \Delta x \Delta z] \quad (4.5) \\ &= -\frac{\delta \sigma_{xx}}{\delta x} \Delta x \Delta y \Delta z + \frac{\delta \tau_{yx}}{\delta y} \Delta x \Delta y \Delta z \end{aligned}$$

Assuming that the fluid is Newtonian and isotropic,  $\sigma_{xx}$  can be related to pressure  $p$  and viscous stresses  $\tau_{xx}$  by

$$\sigma_{xx} = -p + \tau_{xx}$$

For a Newtonian fluid, stress-strain relations can be described as

$$\tau_{xx} = 2\mu \frac{\delta u}{\delta x} \quad \tau_{yx} = \mu \frac{\delta u}{\delta y} \quad (4.6)$$

Where  $\mu$  is the viscosity of the fluid. Combining equations 4.4, 4.5 and 4.6 in the  $x$  direction, and cancelling out the volume term:

$$\rho \frac{Du}{Dt} = -\frac{\delta p}{\delta x} + \mu (\frac{\delta^2 u}{\delta x^2} + \frac{\delta^2 u}{\delta y^2}) + \rho \sum F_b \quad (4.7)$$

Here the acceleration term is the total derivative of  $u$ , defined as the combined local and advection inertial forces, which in two dimensions can be written as

$$\frac{Du}{Dt} = \frac{\delta u}{\delta t} + v \frac{\delta u}{\delta y} + u \frac{\delta u}{\delta x} \quad (4.8)$$

combining equations 4.7 and 4.8 and dividing through by  $\rho$ :

$$\underbrace{\frac{\delta u}{\delta t}}_{local\ acceleration} + v \underbrace{\frac{\delta u}{\delta y} + u \frac{\delta u}{\delta x}}_{convection} = - \underbrace{\frac{1}{\rho} \frac{\delta p}{\delta x}}_{pressure\ gradient} + \underbrace{\nu \left( \frac{\delta^2 u}{\delta x^2} + \frac{\delta^2 u}{\delta y^2} \right)}_{diffusion} + \underbrace{\sum F_b}_{body\ force} \quad (4.9)$$

Where  $\nu$  is kinematic viscosity, defined as  $\frac{\mu}{\rho}$ .

## 4.2 Energy Conservation

Conservation of energy is derived from the first law of thermodynamics, that in a steady flow system the total energy of a control volume remains constant; that inflows and outflows must be equal. This can be expressed analogously to the mass conservation as

$$\frac{DE}{Dt} = \sum \dot{Q} + \sum \dot{W} \quad (4.10)$$

Where  $\dot{Q}$  is heat transfer and  $\dot{W}$  is the rate of work done.  $E$  is energy per unit mass and is expressed as

$E = C_p T$   
 $\frac{DE}{Dt}$  can be expressed similarly to Equation 4.8:

$$\frac{DE}{Dt} = \frac{\delta E}{\delta t} + v \frac{\delta E}{\delta y} + u \frac{\delta E}{\delta x} = C_p \left( \frac{\delta T}{\delta t} + v \frac{\delta T}{\delta y} + u \frac{\delta T}{\delta x} \right) \quad (4.11)$$

For a 2D element, the total energy can therefore be calculated from

$$\rho \frac{DE}{Dt} \Delta x \Delta y = \rho C_p \left( \frac{\delta T}{\delta t} + v \frac{\delta T}{\delta y} + u \frac{\delta T}{\delta x} \right) \Delta x \Delta y \quad (4.12)$$

From Fourier's law of heat conduction, for a 2D system we can write

$$\dot{Q}_x = k A_x \frac{\delta T}{\delta x} = \dot{q}_x A_x = \dot{q}_x \Delta y \quad (4.13)$$

where  $\dot{q}$  is heat flux =  $\dot{Q}/A$

The heat transferred into the element can thus be expressed as

$$[q_x + \frac{\delta q_x}{\delta x}] \Delta y - q_x \Delta y = \frac{\delta q_x}{\delta x} = k \frac{\delta^2 T}{\delta x^2} \Delta x \Delta y \quad (4.14)$$

Figure 4.1: Flow of heat energy through a 2D element

reconstructing equation 4.10 with the inclusion of 4.14, considered also in the y direction, we can cancel out the volume term:

$$\underbrace{\frac{\delta T}{\delta t}}_{local \ acceleration} + u \underbrace{\frac{\delta T}{\delta x} + v \frac{\delta T}{\delta y}}_{convection} = \underbrace{\frac{k}{\rho C_p} \left( \frac{\delta^2 T}{\delta x^2} + \frac{\delta^2 T}{\delta y^2} \right)}_{diffusion} \quad (4.15)$$

### 4.3 Governing Equations

### 4.4 Heat Transfer

### 4.5 Species Transport

# Chapter 5

## Results

### 5.1 Geometry Variations

Figure 5.1 shows 8 coronal slices taken at equidistant spacing across the sagittal axis between the anterior vestibule and the nasopharynx. We see the airway elongate vertically which increases the perimeter but maintaining a relatively constant surface area. This area to perimeter ratio has been cited as an important factor in the development of fluid flow in the nasal cavity. The thinner cavities also tend to exhibit higher wall shear stress. This is because of the steeper velocity gradients, which create stress through the viscosity of air, near the wall. This narrowness is also likely to influence heat and vapour transfer in the cavities; when the cavities are narrower there is less distance for the heat and vapour to travel from the wall to saturate the incoming air, and so it is likely to saturate the airflow more comprehensively. The variation in cavity thickness between the cavities can also be clearly observed in this figure.

Figure 5.1 shows the cross sectional area as a function of normalised distance along the sagittal axis. The distance has been normalised between the entrance to the nostrils and the end of the nasopharynx. A sample of cavities from the pre-existing literature has also been included for comparison. A significant variation can be seen in the average cross sectional area of the models presented in this paper; This variation is most pronounced towards the rear of the cavities. None of the models show quite the same volume as the atrophic rhinitis model, also shown here as Garcia prior to the nasopharynx \*\*\*NOT IN THE CURRENT FIGURE\*\*\*\*, although NC07 is close. The general shape of the curve is reasonably similar for the various models in this paper, with notable exceptions in the Nasopharynx of the NC07 cavity and a larger spike in the vestibule region of NC05. Observations from Figure 3 can be compared with the cross sectional silhouettes from Figure 2, for a clearer understanding of the variations in geometry between the 4 models presented here. The range of cross-sectional areas allows us to observe the relationship between various fluid mechanical properties of the cavity and cavity volume/cross-sectional area.

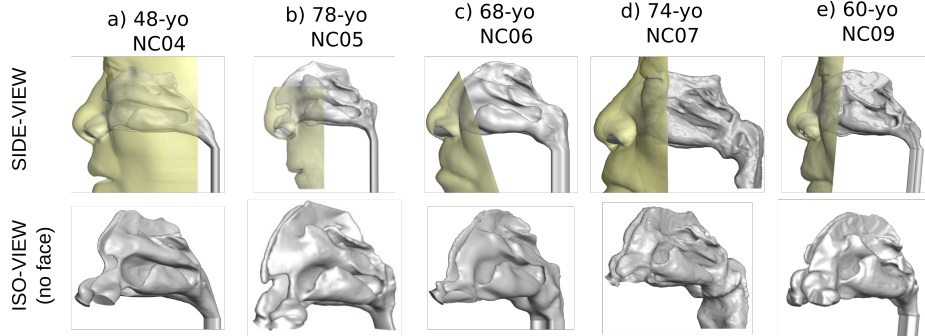


Figure 5.1: geometries of the five cavities

Table 5.1 - 5.3 shows the variation of the volume, surface area and effective diameter respectively, in comparison with models from the literature. The volumes of the four models presented in this paper varied significantly. The largest discrepancies were noted in the pharynx and turbinate regions, with a less marked discrepancy in the vestibular region. The 48 yo is showing greater volume than that seen in the atrophic rhinitis patient from ???. The surface area of the atrophic rhinitis model is also significantly lower, to the extent that the effective diameter, shown in Table 5.3, is larger than the models presented in this paper.

Minimal cross sectional area, shown in Table 5.4, is significant to flow across the cavity???. Here the atrophic rhinitis model shows larger minimal cross sectional area than any of those found in the models presented here, although it is quite close to that of NC07.

## 5.2 Pressure Drop

The pressure drops across the nasal cavities can also be seen in Figure 5.2 to vary in relation to the volume of the nasal cavity. This is in contrast to the experimental findings of [20, 4, 38], whos studies using rhinomanometry showed no significant decrease in pressure across the cavity to accompany the recorded variation in volume. The cause of this discrepancy is unclear. Here the pressure drop is primarily seen across the valve region. Here the nasopharynx has been excluded from the domain; the significant pressure drop across the nasopharynx was inversely proportional to the cross sectional areas of the respective nasal cavities

The pressure drops can be seen in Figure 5.2 to decrease in relation to the volume of the cavity. This fits well with the findings of previous experimental studies looking at pressure drops across nasal cavity models, as can be seen from the comparison with results from [7] and [16], both displayed in figure 5.2.

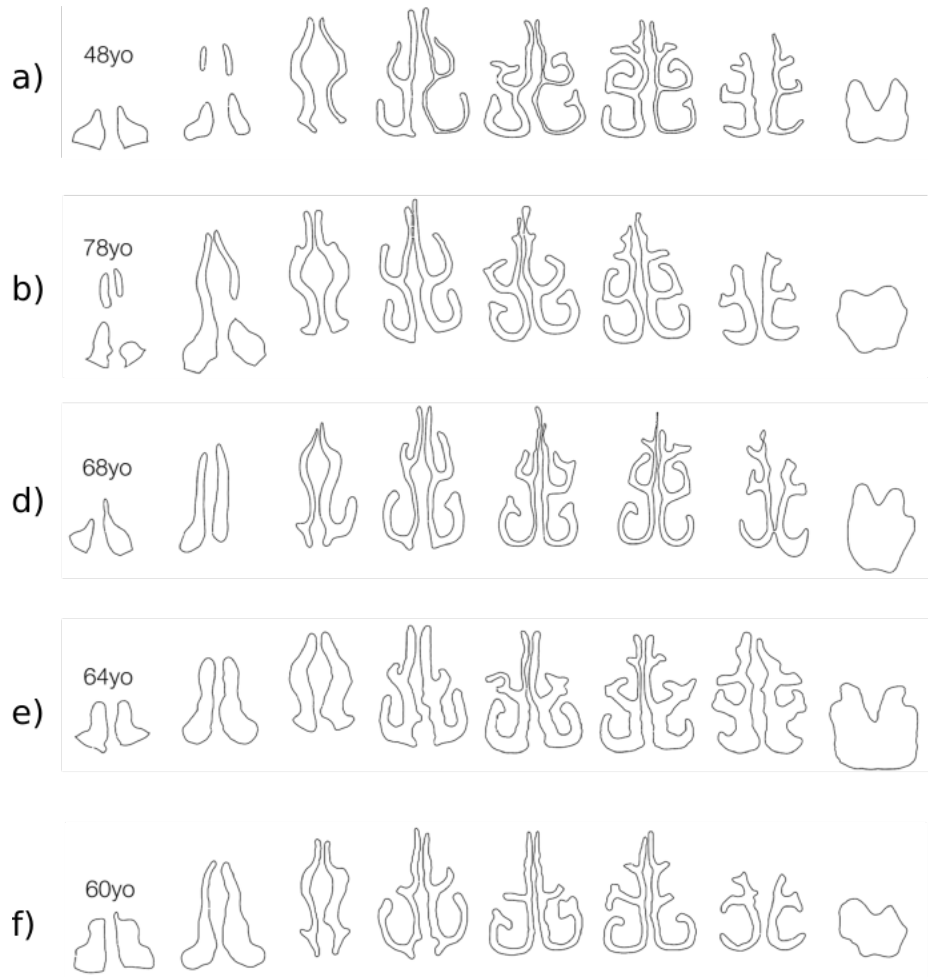


Figure 5.2: silhouettes of the cavities

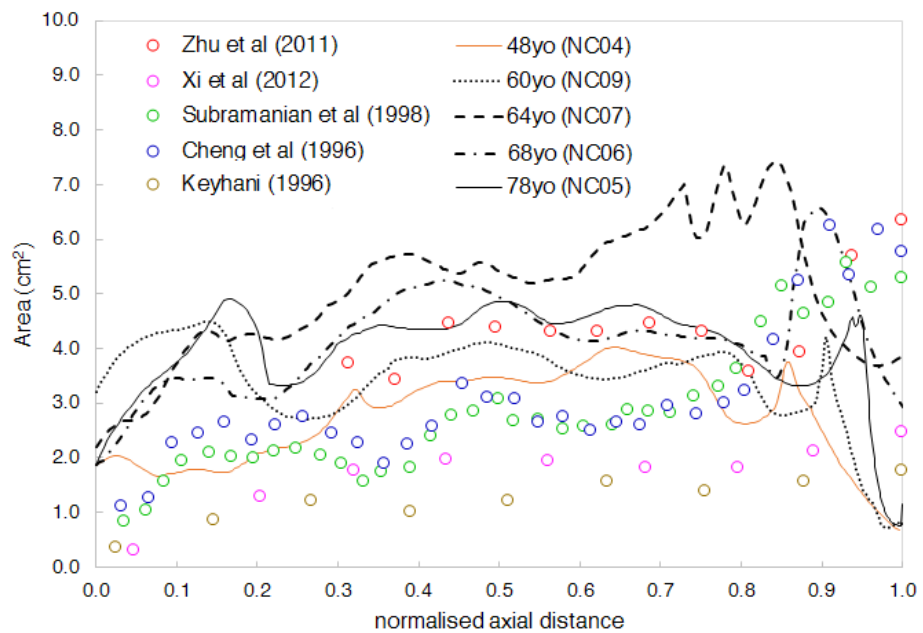


Figure 5.3: area versus distance across the four nasal cavities with a series of examples from the literature



Figure 5.4: Colour coded display of the regional divisions used in tables 5.1, 5.2, 5.3

	<b>NC04</b>	<b>NC05</b>	<b>NC06</b>	<b>NC07</b>	<b>Xi et al.[39]</b>	<b>Garcia et al.[7]</b>
<b>Turbinal region</b>	18.54	22.78	24.62	30.722	12.63	33.66
<b>Nasopharynx</b>	3.84	5.40	12.80	20.09	16.33	10.60
<b>Vestibule</b>	3.10	4.15	2.81	4.21	5.50	2.41
<b>Total</b>	25.48	32.33	40.23	55.07	34.43	47.77

Table 5.1: sectional volume, according to sections as seen in Figure 5.4 ( $cm^3$ )

	<b>NC04</b>	<b>NC05</b>	<b>NC06</b>	<b>NC7</b>	<b>Xi et al.[39]</b>	<b>Garcia et al.[7]</b>
<b>Turbinal region</b>	170.92	174.07	190.44	163.44	112.59	133.50 <sup>1</sup>
<b>Nasopharynx</b>	12.20	12.80	25.23	40.42	40.93	31.46
<b>vestibule</b>	15.71	17.37	12.45	17.92	35.58	-
<b>total</b>	198.82	204.25	228.11	221.79	189.10	164.96

Table 5.2: sectional surface area, according to sections shown in Figure 5.4( $cm^2$ )

	<b>NC04</b>	<b>NC05</b>	<b>NC06</b>	<b>NC7</b>	<b>Xi et al.[39]</b>	<b>Garcia et al.[7]</b>
<b>Turbinal region</b>	0.434	0.52	0.52	0.75	0.45	1.11
<b>Nasopharynx</b>	1.26	1.69	2.03	1.99	1.60	1.35
<b>vestibule</b>	0.79	0.96	0.90	0.94	0.62	-
<b>total</b>	0.51	0.63	0.71	0.99	0.72	1.13

Table 5.3: Effective diameter  $d_{eff} = \frac{4v}{a}$  (cm)

<b>NC04</b>	<b>NC05</b>	<b>NC06</b>	<b>NC07</b>	<b>Xi et al.[39]</b>	<b>Garcia et al.[7]</b>
0.83	1.09	1.80	2.29	1.17	2.54

Table 5.4: Minimal axial cross sectional area ( $cm^2$ )

flowrate	150	300	450	600
48yo	6.80	17.38	34.49	57.99
78yo	3.98	13.08	26.32	43.28
68yo	1.58	5.01	9.67	15.36
64yo	0.31	0.93	1.73	2.67
Inthavong et al 2014	5.87	20.23	43.04	73.95
Kelly et al 2004	7.79	22.51	44.11	71.89
Wen et al 2008	4.85	14.87	30.46	51.29
Weinhold et al. 2004	6.41	17.44	34.65	57.73
Garcia 2007 (AR patient)	4.19	11.69	22.43	36.03

Table 5.5: Variation of pressure drop with flow rate (m/s)

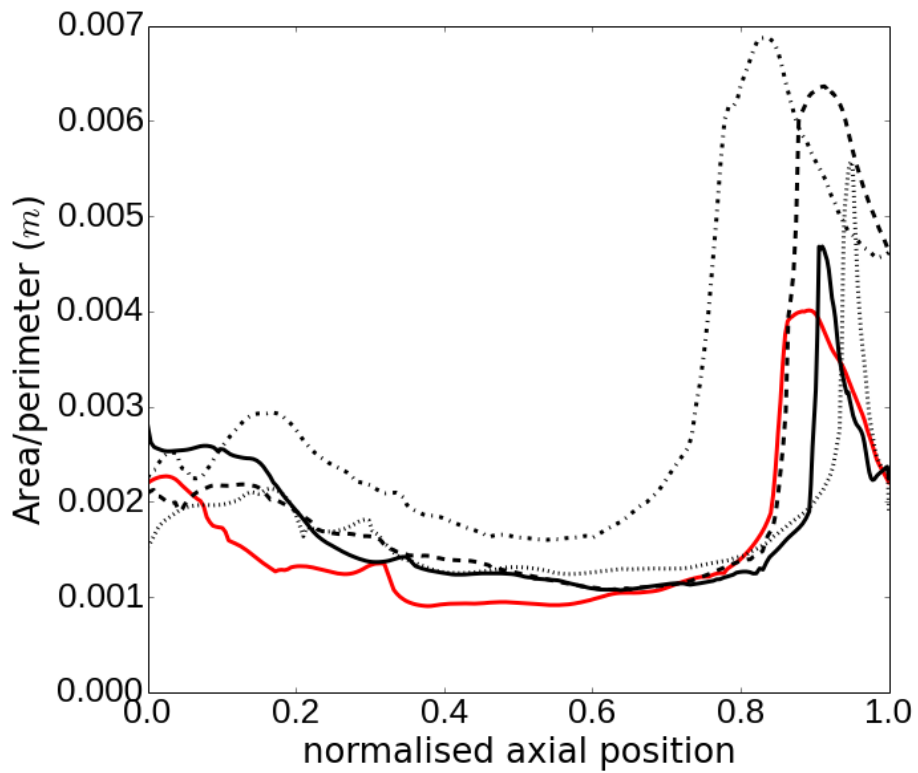


Figure 5.5: area versus distance across the four nasal cavities with a series of examples from the literature

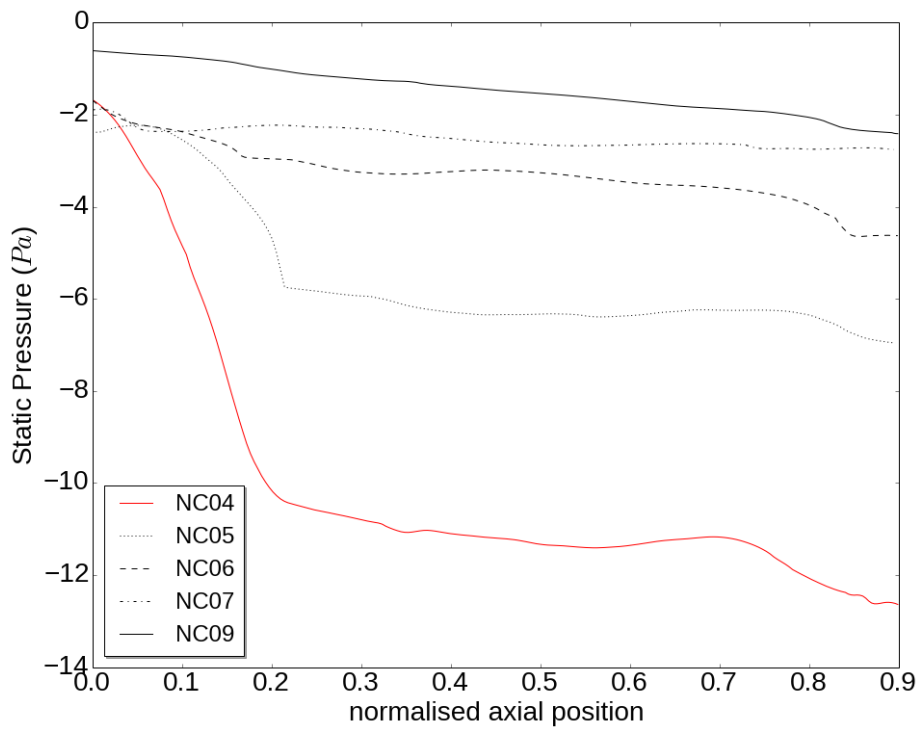


Figure 5.6: area versus distance across the four nasal cavities with a series of examples from the literature

### 5.3 Wall Shear Stress

Figure 5.3 shows the wall shear stress across the five models presented in this paper. The valve region can be seen to be a region of particularly high wall shear across all the models. Also note that the locations of high wall shear vary significantly in the more voluminous cavities

From Figure 5.3, Wall shear stress can be seen to be more pronounced in general in the more voluminous models such as NC04, and in particular this effect is exaggerated in the valve region. Here the wall shear stress is mapped from the nostrils to the entrance to the nasopharynx. The nasopharynx showed more pronounced variations, in particular NC04 showed a significant spike in wall shear stress in the nasopharynx, which is to be expected because of its lower cross sectional area. Note that the sagittal distribution of wall shear stress is much more even in the larger cavities. The valve region - considered of particular significance to the development of flow features within the nasal cavity [20] shows significant variation in wall shear stress concentration, with NC07 and NC09 presenting a very even distribution of wall shear stress, in contrast to NC04 or NC05 which show wall shear more pronounced around the opening from the vestibule. Similar variations can also be seen in the distribution within the turbinal region (Figure 5.3).

Figures 5.3 and 5.3 show the distribution of the wall shear stress around the valve and turbinate regions. The valve region - considered of particular significance to the development of flow features within the nasal cavity [20] shows significant variation in wall shear stress concentration, with NC07 and NC09 presenting a very even distribution of wall shear stress, in contrast to NC04 or NC05 which show wall shear more pronounced around the opening from the vestibule. Similar variations between models can also be seen in the distribution within the turbinal region.

### 5.4 Velocity

Some discrepancies can be observed in the airflow contours between the models of different capacities in Figure 5.4. Note the more even distribution of sagittal airflow in the more voluminous models, particularly notable in NC07 and NC09, when compared with the narrower cavities such as NC04 or NC05. This is particularly prominent in the valve and Turbinal regions. The increasing vorticity seen across the models of increasing volume particularly in the valve region is epitomised in the atrophic rhinitis model from Garcia et al??.

The streamlines show a reduced linearity to the flow as the cavities increase in volume; this is particularly evident in the valve and nasopharynx regions. This varies somewhat from the atrophic rhinitis model, where the most prominent turbulence is in the lower meatus. This is probably related to the significant degeneration seen in the turbinal region of the rhinitis model.

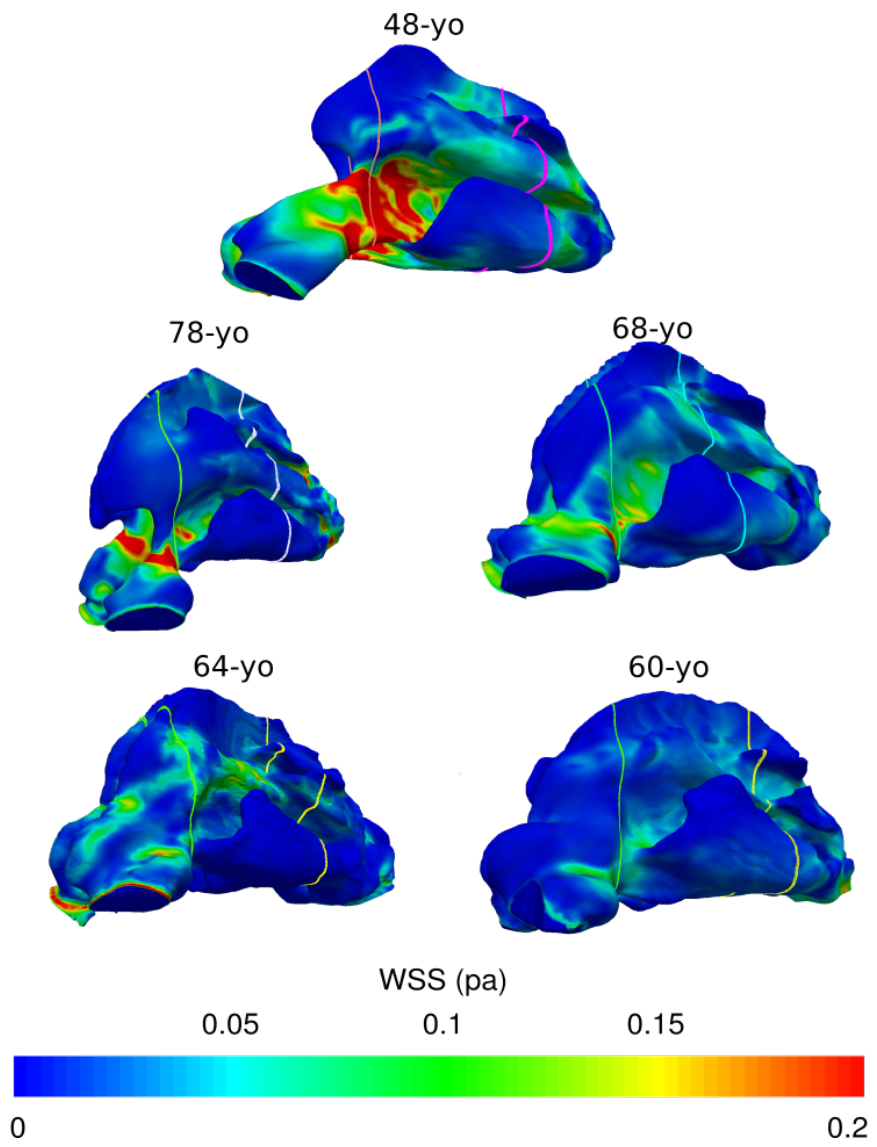


Figure 5.7: isometric views of the five cavities colored by Wall shear stress

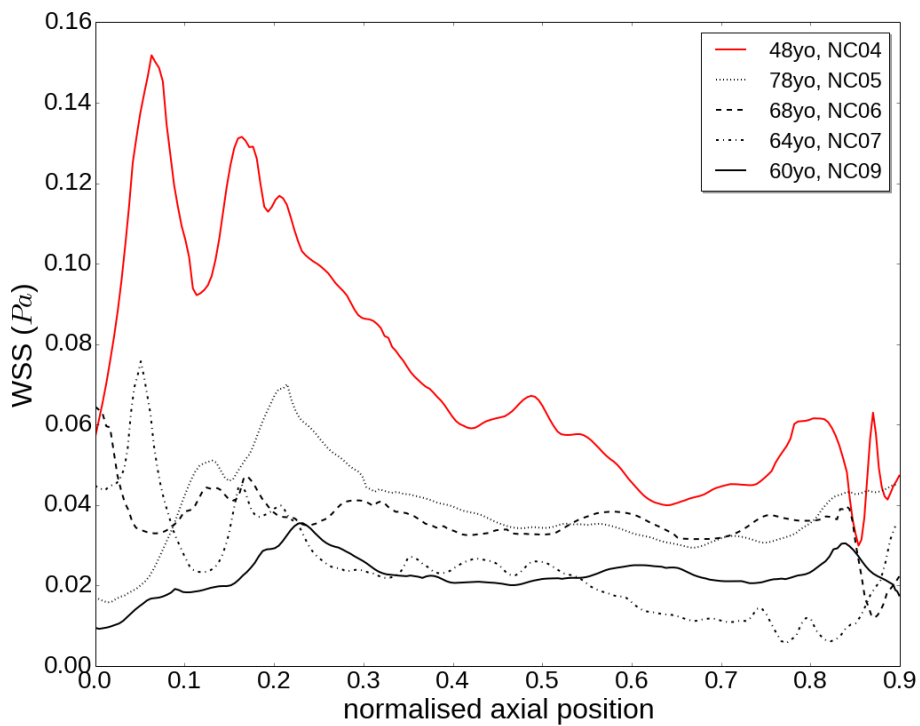


Figure 5.8: coronal area weighted average of wall shear stress plotted as a function of distance from the entrance to the cavity across the saggital axis

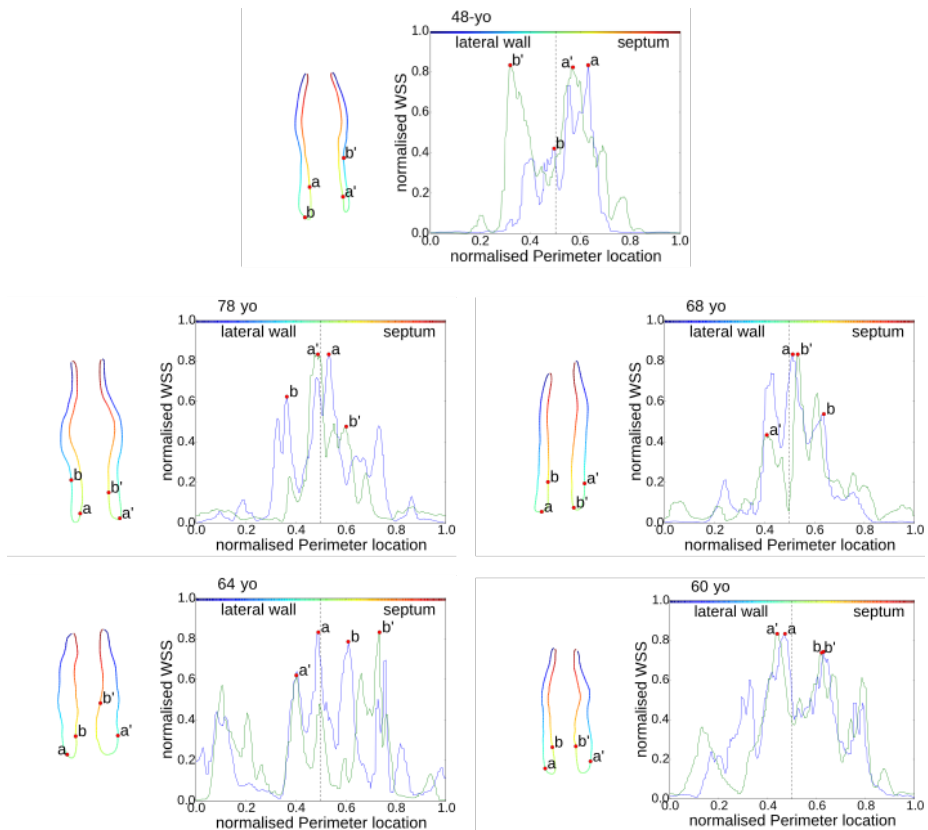


Figure 5.9: wall shear stress around the perimeter of the nasal valve as a function of normalised distance. See the colour scale for precise matching of graph points to location on the cavity wall. Points A and B represent the highest WSS peaks within a given cross section

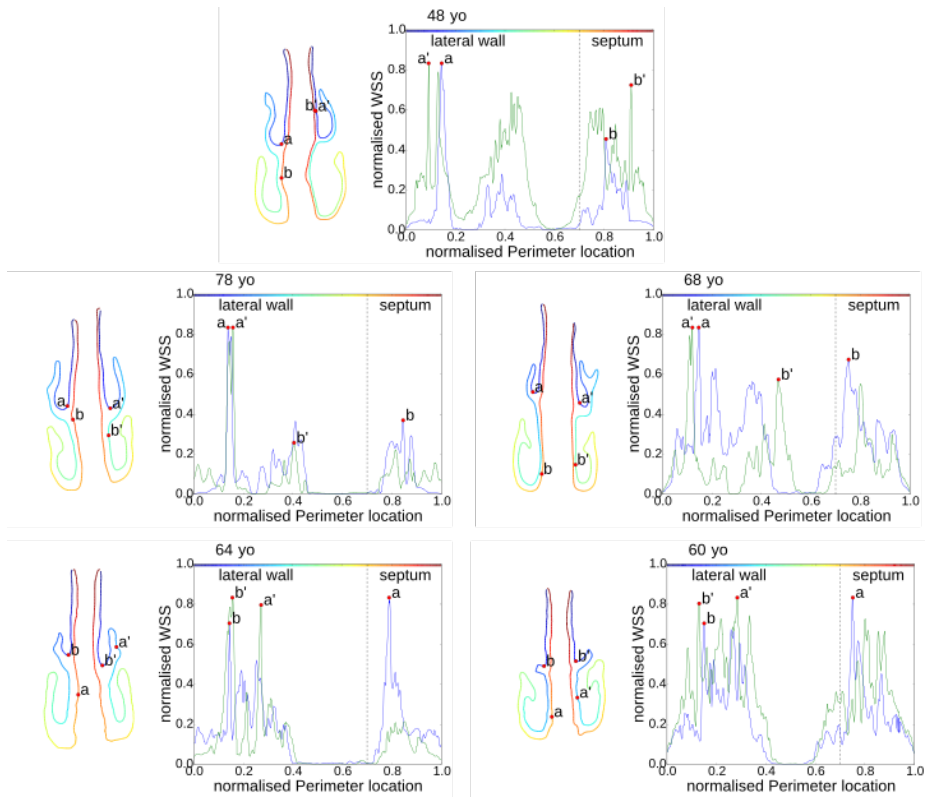


Figure 5.10: wall shear stress around the perimeter of the turbinal region as a function of normalised distance. See the colour scale for precise matching of graph points to location on the cavity wall. Points A and B represent the highest WSS peaks within a given cross section

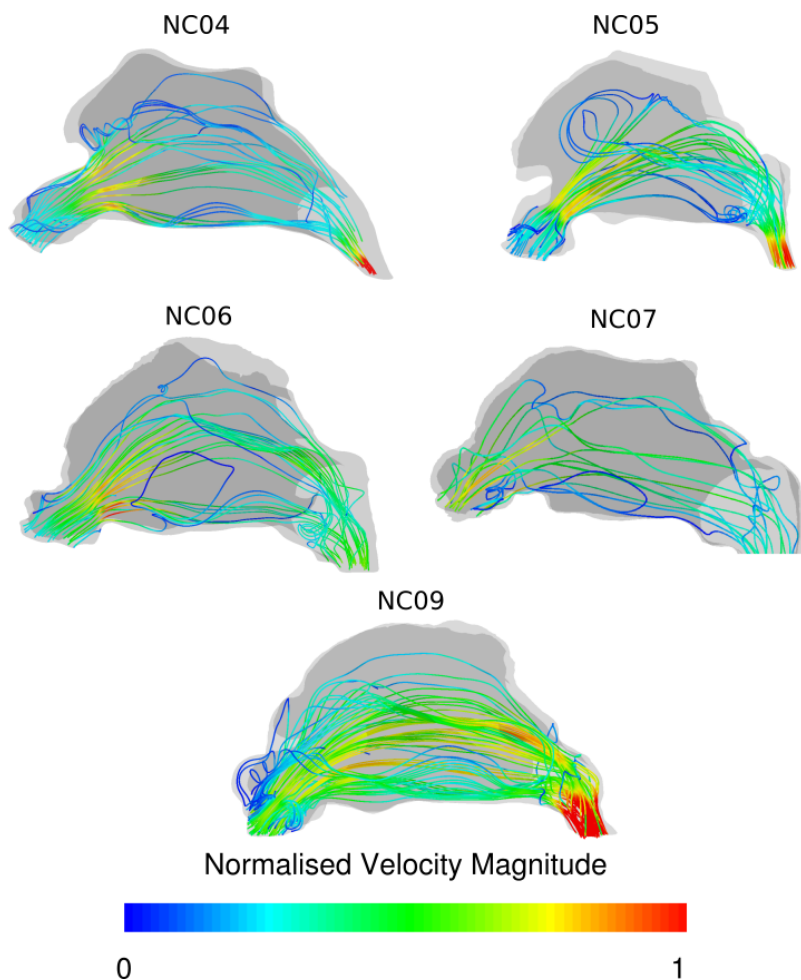


Figure 5.11: streamlines seeded uniformly across the entrance to the nasal cavity, coloured by velocity magnitude, normalised across for the range of each cavity

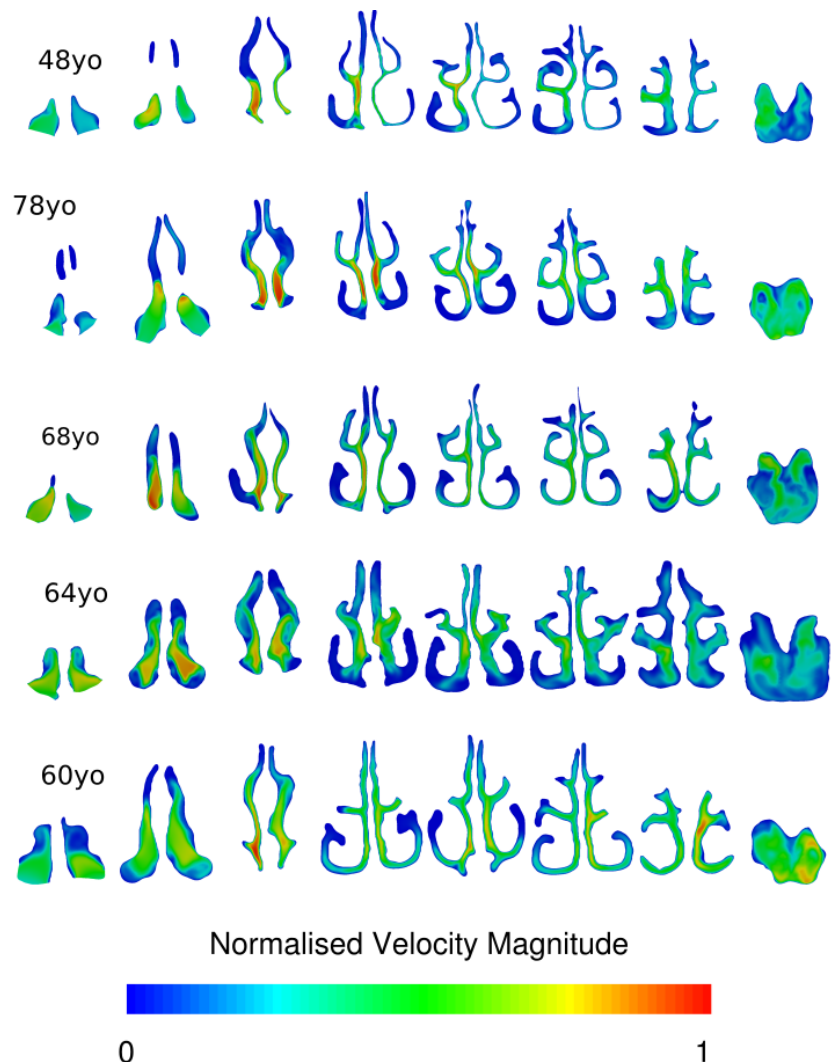


Figure 5.12: Coronal cross sections, taken at 8 equidistant locations across the sagittal axis, coloured by normalised velocity magnitude

## 5.5 Heat and Vapour Transfer

# **Chapter 6**

# **Discussion**

# **Chapter 7**

# **Conclusion**

# Bibliography

- [1] M.A. Burgos, E. Sanmiguel-Rojas, A. Martn-Alcntara, and M.L Hidalgo-Martnez. Effects of the ambient temperature on the airflow across a caucasian nasal cavity. *International Journal for Numerical Methods in Biomedical Engineering*, 30(3):430–445, 2014.
- [2] D. J. Doorly, D. J. Taylor, and R. C. Schroter. Mechanics of airflow in the human nasal airways. *Respiratory Physiology & Neurobiology*, 163(13):100–110, 2008.
- [3] R. Eccles. Nasal airflow in health and disease. *Acta Oto-Laryngologica*, 120(5):580–595, 2000. Biomedical; Continental Europe; Double Blind Peer Reviewed; Editorial Board Reviewed; Europe; Expert Peer Reviewed; Peer Reviewed. No. of Refs: 145 ref. NLM UID: 0370354. PMID: 11039867.
- [4] David R. Edelstein. Aging of the normal nose in adults. *The Laryngoscope*, 106(S81):1–25, 1996.
- [5] David Elad, Sara Naftali, Moshe Rosenfeld, and Michael Wolf. Physical stresses at the air-wall interface of the human nasal cavity during breathing. *Journal of Applied Physiology*, 100(3):1003–1010, 2006.
- [6] David Elad, Michael Wolf, and Tilman Keck. Air-conditioning in the human nasal cavity. *Respiratory Physiology & Neurobiology*, 163(1-3):121 – 127, 2008. Respiratory Biomechanics.
- [7] Guilherme J. M. Garcia, Neil Bailie, Dario A. Martins, and Julia S. Kimbell. Atrophic rhinitis: a cfd study of air conditioning in the nasal cavity. *Journal of Applied Physiology*, 103(3):1082–1092, 2007.
- [8] Qin Jiang Ge, Kiao Inthavong, and Ji Yuan Tu. Local deposition fractions of ultrafine particles in a human nasal-sinus cavity cfd model. *Inhalation Toxicology*, 24(8):492–505, 2012.
- [9] I. Hahn, P.W. Scherer, and M.M. Mozell. Velocity profiles measured for airflow through a large-scale model of the human nasal cavity. *J Appl. Physiol.*, 75(5):2273–2287, 1993.

- [10] O. Hilberg, A. C. Jackson, D. L. Swift, and O. F. Pedersen. *Acoustic rhinometry: evaluation of nasal cavity geometry by acoustic reflection*, volume 66. 1989.
- [11] JAMES HO, KWOK CHAN, WAYNE HU, WAH LAM, LING ZHENG, GEORGE TIPOE, JUNE SUN, RAYMOND LEUNG, and KENNETH TSANG. The effect of aging on nasal mucociliary clearance, beat frequency, and ultrastructure of respiratory cilia. *American Journal of Respiratory and Critical Care Medicine*, 163(4):983–988, Mar 2001.
- [12] Sven Ingelstedt and Nils Gunnar Toremalm. Air flow patterns and heat transfer within the respiratory tract: A new method for experimental studies on models. *Acta Physiologica Scandinavica*, 51(2-3):204–217, 1961.
- [13] Kiao Inthavong, Man Chiu Fung, Xuwen Tong, William Yang, and Jiyuan Tu. High resolution visualization and analysis of nasal spray drug delivery. *Pharmaceutical research*, pages 1–8, 2014.
- [14] L. M. Kalmovich, D. Elad, U. Zaretsky, A. Adunsky, A. Chetrit, S. Sadetzki, S. Segal, and M. Wolf. Endonasal geometry changes in elderly people: Acoustic rhinometry measurements. *Journals of Gerontology Series a-Biological Sciences and Medical Sciences*, 60:396–398, 2005.
- [15] T. Keck, R. Leiacker, A. Heinrich, S. Kuhneman, and G. Rettinger. Humidity and temperature profiles in the nasal cavity. *Rhinology*, 38(167-171), 2000.
- [16] J.T. Kelly, B. Asgharian, J.S. Kimbell, and Wong. B.A. Particle deposition in human nasal airway replicas manufactured by different methods. part 1: Inertial regime particles. *Aerosol Science and Technology*, 38(11):1063–1071, 2004.
- [17] KPWMM Keyhani, PW Scherer, and MM Mozell. Numerical simulation of airflow in the human nasal cavity. *Journal of biomechanical engineering*, 117(4):429–441, 1995.
- [18] J. Lindemann, T. Keck, K. Wiesmiller, B. Sander, H.J. Brambs, G. Rettinger, and P. Pless. A numerical simulation of intranasal air temperature during inspiration. *The Laryngoscope*, 114:1037–1041, 2004.
- [19] Joerg Lindemann, Hans-Juergen Brambs, Tilman Keck, Kerstin M. Wiesmiller, Gerhard Rettinger, and Daniela Pless. Numerical simulation of intranasal airflow after radical sinus surgery. *American Journal of Otolaryngology*, 26(3):175–180, 2005. doi: DOI: 10.1016/j.amjoto.2005.02.010.
- [20] Joerg Lindemann, Diana Sannwald, and Kerstin Wiesmiller. Age related changes in intranasal air conditioning in the elderly. *Laryngoscope*, 118:1472–1475, 2008.

- [21] Joerg Lindemann, Evangelia Tsakiroglou, Iordanis Konstantinidis, and Kerstin Lindemann. Normal aging does not deteriorate nose-related quality of life: Assessment with nose and snot-20 questionnaires. *Auris Nasus Larynx*, 37:303–307, 2010.
- [22] Andreas Lintermann, Matthias Meinke, and Wolfgang Schrder. Fluid mechanics based classification of the respiratory efficiency of several nasal cavities. *Computers in Biology and Medicine*, 43(11):1833 – 1852, 2013.
- [23] Baoshun Ma, Vincent Ruwet, Patricia Corieri, Raf Theunissen, Michel Riethmuller, and Chantal Darquenne. Cfd simulation and experimental validation of fluid flow and particle transport in a model of alveolated airways. *Journal of Aerosol Science*, 40(5):403–414, 2009. doi: DOI: 10.1016/j.jaerosci.2009.01.002.
- [24] R Martin, PS Vig, and DW Warren. Nasal resistance and vertical dento-facial features. In *JOURNAL OF DENTAL RESEARCH*, volume 60, pages 539–539. AMER ASSOC DENTAL RESEARCH 1619 DUKE ST, ALEXANDRIA, VA 22314, 1981.
- [25] T. B. Martonen, Z. Zhang, G. Yue, and C. J. Musante. 3-d particle transport within the human upper respiratory tract. *Journal of Aerosol Science*, 33(8):1095–1110, 2002.
- [26] S. Naftali, M. Rosenfeld, M. Wolf, and D. Elad. The air-conditioning capacity of the human nose. *Annals of Biomedical Engineering*, 33:545–553, 2005.
- [27] S. Naftali, R.C. Schroter, J. Shiner, and D. Elad. Transport phenomena in the human nasal cavity: A computational model. *Annals of Biomedical Engineering*, 26:831–839, 1998.
- [28] ML Nuckols, JL Zumrick, and CE Johnson. Heat and water vapor transport in the human upper airways at hyperbaric conditions. *Journal of biomechanical engineering*, 105(1):24–30, 1983.
- [29] H. Shi, C. Kleinstreuer, and Z. Zhang. Laminar airflow and nanoparticle or vapor deposition in a human nasal cavity model. *Journal Biomech. Eng.*, 128(5):697–706, 2006.
- [30] H Stammberger. History of rhinology: anatomy of the paranasal sinuses. *Rhinology*, 27(3):197–210, 1989.
- [31] Corbin D Sullivan, Guilherme JM Garcia, Dennis O Frank-Ito, Julia S Kimbell, and John S Rhee. Perception of better nasal patency correlates with increased mucosal cooling after surgery for nasal obstruction. *Otolaryngology—Head and Neck Surgery*, page 0194599813509776, 2013.

- [32] D. J. Taylor, D. J. Doorly, and R. C. Schroter. Inflow boundary profile prescription for numerical simulation of nasal airflow. *JOURNAL OF THE ROYAL SOCIETY INTERFACE*, 7:515–527, 2010.
- [33] J. Tu, G.H. Yeoh, and C. Liu. *Computational fluid dynamics: a practical approach*. Butterworth-Heinemann, 2008.
- [34] Victoria E Varga-Huettner and Jayant M Pinto. Physiology of the aging nose and geriatric rhinitis. In *Nasal Physiology and Pathophysiology of Nasal Disorders*, pages 165–181. Springer, 2013.
- [35] I. Weinhold and G. Mlynksi. Numerical simulation of airflow in the human nose. *European Archive Otorhinolaryngology*, 261:452–455, 2004.
- [36] Jian Wen, Kiao Inthavong, Jiyuan Tu, and Simin Wang. Numerical simulations for detailed airflow dynamics in a human nasal cavity. *Respiratory Physiology & Neurobiology*, 161(2):125–135, 2008.
- [37] J.F. Wendt and J.D. Anderson. *Computational fluid dynamics: an introduction*. Springer, 2009.
- [38] Si Whan Kim, Ji-Hun Mo, Jeong-Whun Kim, Dong-Young Kim, Chae-Seo Rhee, Chul Hee Lee, and Yang-Gi Min. Change of nasal function with aging in korean. *Acta Oto-Laryngologica*, 127(S558):90–94, 2007.
- [39] Jinxiang Xi, Ariel Berlinski, Yue Zhou, Bruce Greenberg, and Xiawei Ou. Breathing resistance and ultrafine particle deposition in nasal-laryngeal airways of a newborn, an infant, a child, and an adult. *Annals of Biomedical Engineering*, 40:2579–2595, 2012.
- [40] Jinxiang Xi, JongWon Kim, Xiuhua A. Si, Wei Chung Su, and Yue Zhou. Effects of the facial interface on inhalation and deposition of micrometer particles in calm air in a child airway model. *Inhalation Toxicology*, 26:492–505, 2014.
- [41] G. Xiong, J. Zhan, K. Zuo, J. Li, L. Rong, and G. Xu. Numerical flow simulation in the post-endoscopic sinus surgery nasal cavity. *Medical and Biological Engineering and Computing*, 46(11):1161–1167, 2008.
- [42] Shen Yu, Xiu-zhen Sun, and Ying-xi Liu. Numerical analysis of the relationship between nasal structure and its function. *The Scientific World Journal*, 2014, 2014.
- [43] Jian Hua Zhu, Heow Pueh Lee, Kian Meng Lim, Shu Jin Lee, and De Yun Wang. Evaluation and comparison of nasal airway flow patterns among three subjects from caucasian, chinese and indian ethnic groups using computational fluid dynamics simulation. *Respiratory Physiology & Neurobiology*, 175(1):62–69, 2011.